Journal of the Taiwan Institute of Chemical Engineers 44 (2013) 660–669

Contents lists available at SciVerse ScienceDirect

Journal of the Taiwan Institute of Chemical Engineers

journal homepage: www.elsevier.com/locate/jtice

Photocatalytic activity and mechanism of nano-cubic barium titanate prepared by a hydrothermal method

Wenlian William Lee [b,c], Wen-Hsin Chung [d], Wu-Sheng Huang [a], Wei-Chieh Lin [a], Wan-Yu Lin [d], Yu-Rou Jiang [a], Chiing-Chang Chen [a,*]

[a] Department of Science Application and Dissemination, National Taichung University of Education, Taichung 40306, Taiwan
[b] Department of Occupational Safety and Health, Chung-Shan Medical University, Taichung 40201, Taiwan
[c] Department of Occupational Medicine, Chung Shan Medical University Hospital, Taichung 40201, Taiwan
[d] Department of Plant Pathology, National Chung Hsing University, Taichung 40201, Taiwan

ARTICLE INFO

Article history:
Received 1 September 2012
Received in revised form 25 December 2012
Accepted 6 January 2013
Available online 13 March 2013

Keywords:
$BaTiO_3$
Nanocubic
Crystal violet
Hydrothermal
Photocatalytic

ABSTRACT

This paper presents a study on the efficiency and mechanisms underlying the photo-catalytic degradation of crystal violet (CV) using nano-cubic barium titanate ($BaTiO_3$). This study used P25-TiO_2 as a starting material for the synthesis of $BaTiO_3$, due to of its low cost, stability, and nontoxicity, compared with titanium alkoxide. The $BaTiO_3$ was first synthesized using the autoclave hydrothermal method under alkaline condition with P25-TiO_2 and $Ba(OH)_2{\cdot}8H_2O$ as starting materials, using various NaOH concentrations, reaction durations, and reaction temperatures. The characterization of the resulting $BaTiO_3$ was confirmed by SEM-EDS, powder XRD, HR-XPS, FT-IR, DR-UV, and BET. The band gap of nanocubic $BaTiO_3$ is estimated to be 2.93–3.05 eV and the lower band gap has a positive effect on photocatalytic activity. The photo-degradation efficiency of CV dye by $BaTiO_3$ was measured under UV light irradiation with various pH reaction media in dark room conditions for comparison. Degradation intermediates were separated using HPLC-PDA-ESI/MS to identify the possible mechanism involved in photo-degradation according to variations in the concentration ratio of intermediates during the course of the reaction.

1. Introduction

The elimination of toxic chemicals from wastewater is a crucial subject in pollution control. The textile industry contributes considerably to the problem of pollution due to dumping or the accidental discharge of dye wastewater into waterways, which has a major impact on the quality and aesthetics of water resources. The World Bank estimates that 17–20% of all industrial water pollution comes from the dyeing and treatment of textiles [1,2]. This represents an appalling environmental challenge for clothing designers and other textile manufacturers. The enormous quantity of dyes used in the dyeing stage of textile manufacturing represents an increasing environmental danger due to their refractory carcinogenic nature. In particular, triphenylmethane dyes are heavily consumed in paper, leather, cosmetics, and food industries in the coloring of oils, fats, waxes, varnish, and plastics [3]. The photocytotoxicity of triphenylmethane dyes, based on the production of the reactive oxygen species, has been intensively studied with regard to photodynamic treatment [4]. However, there is considerable concern about the thyroid peroxidase-catalyzed oxidation of triphenylmethane dyes because the reaction could potentially form various *N*-de-alkylated aromatic amines, the structure of which is similar to aromatic amine carcinogens [5]. Hence, a new treatment method must be developed to overcome the problem of toxicity caused by dye wastewater. Recently, the application of semiconductors in the advanced oxidation process (AOP) has attracted considerable interest in the treatment of dye wastewater, owing to its high degradation efficiency, low toxicity, and physical and chemical properties. AOP refers to a set of chemical treatment procedures designed to remove organic and inorganic materials from wastewater through oxidation.

In recent years, environmental issues have become increasingly important. Numerous treatment technologies have been developed for environmental remediation, such as adsorption methods, ion-exchange methods, membrane separation, and photocatalysis [1,6]. In particular, photocatalysis has been intensively studied due to its simplicity, low cost, and high removal efficiency. Semiconductor photocatalysis has received considerable attention for use in counteracting environmental degradation and as a potential solution to the worldwide energy shortage. Since titania was first described as a catalyst for photochemical water splitting, a variety

* Corresponding author. Tel.: +886 4 2218 3406; fax: +886 4 2218 3560.
E-mail addresses: ccchen@mail.ntcu.edu.tw, ccchen@ms3.ntcu.edu.tw (C.-C. Chen).

1876-1070/$ – see front matter © 2013 Taiwan Institute of Chemical Engineers. Published by Elsevier B.V. All rights reserved.
http://dx.doi.org/10.1016/j.jtice.2013.01.005

of semiconducting particles have been used as photocatalysts to decompose water containing organic pollutants [7] and for hydrogen evolution [8]. TiO_2 is broadly used as a photocatalyst for the degradation of a wide range of organic pollutants due to its nontoxicity, photochemical stability, and low cost [7–9]. Compared to TiO_2, titanates exhibit inherent chemical reactivity, which is beneficial for designing complex titanate-based composites. To date, a wide range of titanate-based photocatalysts have been achieved, such as $CaTiO_3$ [10], $SrTiO_3$ [11], $BaTiO_3$ [12], In_2TiO_5 [13], $MnTiO_3$ [14] and $CdTiO_3$ [15]. Some of these display good photocatalytic activity and chemical stability. The fabrication of perovskites (ABO_3) is of particular scientific and technological interest due to their ferroelectric, pyroelectric, piezoelectric, dielectric, and catalytic properties. In this study, we attempted to synthesize alkaline earth titanate $BaTiO_3$ with a variable morphology by taking advantage of the high activity of titanate nanopowders.

$BaTiO_3$ (BTO) has great potential for technological applications in ferroelectricity, microelectronics, optoelectronics, and photocatalysis [16]. It has mostly been used in the production of devices such as multilayer ceramic capacitors, high-density optical data storage, ultrasonic transducers, and piezoelectric devices. $BaTiO_3$ exists in various crystallographic structures, of which the tetragonal and cubic polymorphs are the most widely studied. Although the tetragonal polymorph is thermodynamically stable at room temperature, most synthesis routes result in a cubic structure.

Stimulated by fundamental scientific study and technological application, researchers have synthesized $BaTiO_3$ through a variety of methods, including conventional solid-state reactions, hydrothermal synthesis [12], the sol–gel method [17], inverse micelle microemulsion, molten salt synthesis [18], the nonaqueous route [19], and the biological synthetic technique [20]. Recently, ferroelectric materials have emerged from a hydrothermal reaction as an important conformation. Single-crystalline $BaTiO_3$ nanorods have been produced through a solution-based decomposition of bimetallic alkoxide precursors [21]. Tetragonal $BaTiO_3$ has been formed using $TiCl_4$ with $Ba(OH)_2$ in a microwave hydrothermal process [22]. Hydrothermal treatment of layered titanate in $Ba(OH)_2$ aqueous solution has resulted in $BaTiO_3$ with a variety of nanostructures [23]. Thus, it would be highly desirable to develop a standard approach to fabricate $BaTiO_3$ with controllable size and morphology.

Crystal violet (CV) is a cationic triphenylmethane dye, which has been extensively used as a commercial dye in textiles, biological stain, antimicrobial agent, dermatological agent, veterinary medicine, and targetable sensitizer [24]. However, CV in wastewater not only causes coloration, but also harms aquatic life. Furthermore, its presence in drinking water poses a potential threat to human health. Thus, there exists a need for the development of efficient, inexpensive dye wastewater treatment processes to deal with this issue.

However, less attention has been paid to the study of the underlying mechanism involved in degradation or the identification of major transient intermediates, which have recently been recognized as important elements in these processes, particularly in view of their practical applications. No previous mechanistic studies on $BaTiO_3$-assisted photocatalytic degradation for CV dye under UV irradiation have been reported. Compared with $Ti(OR)_4$ (R = alkyl group), P25-TiO_2 is used as a starting material for the synthesis of metal titanate because of its nontoxicity, stability, and low cost. In this work, P25-TiO_2, $Ba(OH)_2{\cdot}8H_2O$, and NaOH were first used as precursors in the successful preparation of $BaTiO_3$ nanocubes via an autoclave hydrothermal treatment at various reaction temperatures and times.

2. Experimental

2.1. Materials and preparation of photocatalysts

Chloride salt of crystal violet (TCI), P25-TiO_2 (Degussa Co. Ltd; *ca.* 80% anatase, 20% rutile; particle size, *ca.* 20–30 nm; BET area, *ca.* 55 m^2/g), $Ba(OH)_2{\cdot}8H_2O$ (Katayama Co. Ltd.; assay $\geq$ 97%), NaOH and CH_3COONH_4 (Osaka Co. Ltd.; guaranteed reagent), HNO_3 (JIS Co. Ltd.; extra pure), acetone (Merck Co. Ltd.; HPLC-grade), and CH_3OH (J.T. Baker Co. Ltd.; HPLC-grade) were used as starting materials. The de-ionized water used in this study was purified using a Milli-Q water ion-exchange system (Millipore Co.) for a resistivity of 1.8×10^7 Ω-cm. The P25-TiO_2 nanoparticles were supplied by Degussa. The BTO nanopowders were synthesized in a beaker by adding 0.1 g P25-TiO_2 and 10 mL NaOH aqueous solution (1, 3, 5, and 10 M) respectively to 0.35 g $Ba(OH)_2{\cdot}8H_2O$. The mixture was transferred to a Teflon-lined autoclave (capacity: 23 mL) and heated to 100 °C (or 130 °C, 150 °C, 180 °C) for 24 h (or 48 h, 72 h). The material was washed with distilled water, filtered and finally dried in air at 60 °C. A variety of reaction conditions were employed (including various concentrations of NaOH, reaction times, and temperature) as shown in Table 1, namely BA-3-24-130 to BA-5-48-180 for $BaTiO_3$ samples, respectively.

2.2. Instruments and characterization

The prepared catalysts were examined using both energy dispersive spectroscopy (EDS) and a high resolution X-ray photoelectron spectrometer (HR-XPS). X-ray powder diffraction (XRD) patterns were recorded on a MAC Sience, MXP18 X-ray diffractometer with Cu Kα radiation, operated at 40 kV and 80 mA. An HR-XPS measurement was carried out with ULVAC-PHI XPS. Al Kα radiation was generated using a voltage of 15 kV. Field emission scanning electron microscopy (FE-SEM) measurements were carried out using a field-emission microscope (JEOL JSM-7401F) at an acceleration voltage of 15 kV. At the temperature of liquid nitrogen, the specific surface area of the BET samples was measured using an automatic system (Micromeritics Gemini 2370C) with nitrogen gas as the adsorbate. Fourier transform infrared (FT-IR) spectra were collected using a Nicolet 380 FT-IR spectrometer. UV–vis diffuse reflectance spectra were recorded on a Scinco SA-13.1 spectrophotometer at room temperature. A Waters ZQ LC/MS system, equipped with a binary pump, a photodiode array detector, an autosampler, and a micromass detector, was used for separation and identification.

2.3. Photocatalytic procedure and analysis

Aqueous suspensions of CV (100 mL, 10 ppm) and catalyst powders were placed in a Pyrex flask. The pH value of the suspensions was adjusted by the addition of either NaOH or HNO_3

Table 1
Summary of samples prepared using hydrothermal treatment with various concentrations of NaOH, synthesis duration, and temperature.

Catalyst code	Ti precursor	Ba precursor	NaOH concentration (M)	Synthesis time (h)	Synthesis temperature (°C)
BA-3-24-130	TiO_2	$Ba(OH)_2$	3	24	130
BA-5-24-130	TiO_2	$Ba(OH)_2$	3	24	130
BA-10-24-130	TiO_2	$Ba(OH)_2$	10	24	130
BA-5-48-130	TiO_2	$Ba(OH)_2$	5	48	130
BA-5-72-130	TiO_2	$Ba(OH)_2$	5	72	130
BA-5-48-100	TiO_2	$Ba(OH)_2$	5	48	100
BA-5-48-150	TiO_2	$Ba(OH)_2$	5	48	150
BA-5-48-180	TiO_2	$Ba(OH)_2$	5	48	180

solution. Prior to irradiation, the suspensions were magnetically stirred in the dark for approximately 30 min to establish adsorption/desorption equilibrium between the dye, and the surface of the catalyst under ambient air-equilibrated conditions. Irradiation was carried out using two UV-365 nm lamps (15 W). At given irradiation time intervals, 5 mL aliquots were collected, centrifuged, and then filtered through a Millipore filter to remove catalyst particulates. The filtrates were analyzed by HPLC-ESI–MS following the readjustment of the chromatographic conditions to make the mobile phase compatible with the working conditions of the mass spectrometer.

3. Results and discussion

3.1. Effect of NaOH concentration

When the formation of crystalline $BaTiO_3$ powders under hydrothermal conditions is complete, the resulting particles grow through Ostwald ripening, which is the final stage of a first-order phase transformation process. The first stage of nucleation is the result of a high degree of super-saturation of the solution; the second stage of particle growth results from the deposition of solute, which leads to a decrease in super-saturation and yields a distribution of particles of various sizes. Ostwald ripening or particle coarsening occurs when the super-saturation has become very light. The driving force behind coarsening is a reduction in the total surface free energy resulting from the growth of larger particles at the expense of the dissolution of smaller ones [25].

It is assumed that the coarsening of hydrothermal $BaTiO_3$ is controlled by a reversible interface reaction, considering the drastic decrease in the viscosity of water under hydrothermal conditions. From the thermodynamic data provided by Lencka and Riman [26], the calculations indicate that in a basic solution with temperatures above 200 °C, soluble Ti species exist mainly in the forms of $Ti(OH)_4$ and $HTiO_3^-$, and dissolved Ba species exist as $BaOH^+$ and Ba^{2+}. Considering that the number of reactant molecules involved in an elementary reaction seldom exceeds 2, the reversible dissolution and deposition reactions at the surface of $BaTiO_3$ particles are assumed to be

$$BaTiO_{3(s)} + H_2O \underset{k_g}{\overset{k_d}{\rightleftharpoons}} BaOH^+ + HTiO_3^-$$

where k_d and k_g are the rate coefficients of dissolution and deposition, respectively. k_d probably depends on the activity of particles and hence is a function of the radius R of the particle. By contrast, k_g is independent of R, because the reactants involved are in the liquid phase [25]. For convenience, the $BaTiO_3$ particle is assumed to be chemically stoichiometric and to have a spherical shape. Because the coarsening is controlled by interface reaction, the concentrations of solutes in the solution are assumed to be uniform [27].

The ratio of Ba/Ti was chosen to be greater than 1 to avoid contaminating $BaTiO_3$(s) with excess TiO_2(s) under the conditions of hydrothermal synthesis [28]. Furthermore, Ba/Ti > 1 increases the pH of the solution, which is an important thermodynamic variable in the synthesis of perovskite materials, and helps to avoid the need for additional alkaline mineralizer to facilitate the formation of $BaTiO_3$. According to the thermodynamic calculations of stability for the hydrothermal Ba–Ti system, high pH and Ba/Ti > 1 are necessary for the synthesis of high purity $BaTiO_3$ crystals.

$BaTiO_3$ powder, prepared with NaOH concentration in the range of 3–10 M with various reaction times and temperatures, was characterized using XRD, SEM-EDS, XPS, FT-IR, BET, and DR-UV techniques. The results are summarized in Table 2. XRD patterns of as-synthesized $BaTiO_3$ (Fig. A.1 of supporting information) with NaOH concentrations of 3, 5, and 10 M showed characteristic peaks of both cubic $BaTiO_3$ (JCPDS File No. 74-1963) and $BaCO_3$ (JCPDS File No. 41-0373) [29]. A small amount of $BaCO_3$ contamination was noted in nearly all of the samples due to the introduction of airborne CO_2, which dissolved as CO_3^{2-} and reacted with Ba^{2+} to form $BaCO_3$ during post treatment [30]. The formation of $BaCO_3$ observed in this work is quite common in hydrothermal processing, as $BaCO_3$ can precipitate at lower pH values than those required by $BaTiO_3$. According to the thermodynamic stability diagram of Ba–Ti systems, $BaCO_3$ precipitates at lower pH values than those required to precipitate $BaTiO_3$ [28]. The XRD results of the as-synthesized $BaTiO_3$ illustrate the presence of weak peaks at $2\theta = 24^\circ$, 35°, 42°, which corresponds to the phase of $BaCO_3$. The $BaTiO_3$ peaks are very sharp, indicating that the crystalline structure is well developed. The effect of NaOH concentration on the crystal structure and characterization of $BaTiO_3$ is summarized in Table 2. It can be observed that, even with increased concentrations of NaOH, the intensity of $BaTiO_3$ diffraction peaks increased slightly, indicating the presence of an increased crystalline phase content. A slight increase in the intensity of the cubic phase with NaOH concentration may be caused by the removal of barium vacancies (charge compensator of OH^- defect) due to excess barium content. This is the result of reactions between CO_2 from air and alkaline earth hydroxides during the process. Another possible source of carbonate is the raw barium hydroxides, which can react with CO_2 in the air during storage.

Fig. A.2 shows SEM images of $BaTiO_3$ samples prepared at NaOH concentrations of 3, 5 and 10 M. The particles agglomerated in a spherical shape with roughly 10–150 nm diameters and a small quantity of cubic crystalline phase [31]. A possible mechanism underlying the formation of $BaTiO_3$ through hydrothermal synthesis is dissolution-precipitation [31], in which a chemical equilibrium exists between TiO_2 and $Ti(OH)_x^{4-x}$. Fig. A.2 shows an increase in the particle size of $BaTiO_3$ with an increase in NaOH concentration, which is in accord with the mechanism of dissolution-precipitation. $Ti(OH)_x^{4-x}$, which is a highly active species, is capable of combining with Ba^{2+} to form a new nucleus,

Table 2
Physical and chemical properties of prepared $BaTiO_3$.

Catalyst code	EDS element atomic ratio (%)			XPS element atomic ratio (%)			E_g(eV)	Specific surface area (m^2/g)	Pore size (Å)	Pore volume (cm^3/g)
	Ba	Ti	O	Ba	Ti	O				
BA-3-24-130	7.42	13.22	51.90	–	–	–	2.95	–	–	–
BA-5-24-130	5.29	8.64	67.05	8.59	13.16	58.51	3.03	17.88	11.51	0.01
BA-10-24-130	13.10	13.02	73.88	–	–	–	3.02	–	–	–
BA-5-48-130	6.68	13.37	79.95	7.40	17.80	56.57	3.00	20.35	11.90	0.01
BA-5-72-130	8.24	14.35	77.40	9.39	17.54	56.65	3.02	18.51	11.52	0.01
BA-5-48-100	21.28	31.49	47.24	–	–	–	2.93	–	–	–
BA-5-48-150	9.14	10.78	80.08	–	–	–	3.01	–	–	–
BA-5-48-180	8.71	13.63	77.66	–	–	–	3.05	–	–	–

and hence, with an increase in NaOH concentration, the chance of forming a new nucleus by $Ti(OH)_x^{4-x}$ increases, leading to an increase in the particle size of $BaTiO_3$. It can be concluded that the phase formation of cubic $BaTiO_3$ occurs when P25-TiO_2 was used as the $Ti(OH)_x^{4-x}$ precursor. Moreover, the primary particle size of $BaTiO_3$ prepared using lower concentrations of NaOH is smaller than that prepared using higher concentrations of NaOH, which can be ascribed to the smaller particle size of $BaTiO_3$ prepared by the $Ti(OH)_x^{4-x}$ precursor [28]. The agglomeration of $BaTiO_3$ nanoparticles at higher NaOH concentrations promotes the growth of the cubic phase.

In Fig. A.3, the adsorption reaction resulted in a decrease of approximately 46% in the CV concentration after 48 h; in the photocatalytic reaction, the CV was completely decomposed after 48 h. A comparison with TiO_2 suggests that the photocatalytic activity of BTO nanoparticles is relatively good. With continued development, these kinds of nanomaterials have the potential to become commercial photocatalysts. In the following experiment, we selected $BaTiO_3$ produced with a concentration of 5 M NaOH as the optimal photocatalyst.

3.2. Influence of synthesis duration

The influence of synthesis duration on the formation of crystalline $BaTiO_3$ was also studied by performing experiments with various reaction durations ranging from 24 to 48 h at 130 °C with [NaOH] = 5 M. The XRD patterns in Fig. 1 confirm the cubic phase of $BaTiO_3$. With an increase in reaction time from 24 to 72 h, the sharpness and cubic size increased, indicating an increase in the crystallinity of the cubic phase with an increase in the particle size of $BaTiO_3$. In the early stage of the reaction, hydroxide ions produce more nuclei and formed smaller particles, which grew over a prolonged period. The SEM micrographs in Fig. 2 indicate a considerable difference in the morphology between 24 and 72 h. The crystalline form at shorter periods of time (24 h) primarily results from particles agglomerating in a spherical shape. The cluster size enlarged with an extension in processing, resulting in a cubic crystalline shape.

In Table 2, X-ray photoelectron spectroscopy and energy dispersive spectroscopy results reveal mismatches in the stoichiometry and differences in the chemical composition of the surfaces among the various samples. Fig. 3 displays the Ba $3d_{5/2}$, O 1s and Ti 2p photoemission spectra. The binding energy of the Ti $2p_{3/2}$ peak (458.053–458.156 eV) is in good agreement with previous XPS studies on $BaTiO_3$ [32]. The O 1s spectra revealed several components. The O 1s spectrum of the samples can be deconvoluted into a component in the energy range of 529.328–529.557 eV, which corresponds to $BaTiO_3$, and a component at 531.256 eV, which was previously identified with hydroxyl groups typical of adsorbed water [32]. On the other hand, the Ba $3d_{5/2}$ spectra indicate that barium is in a different chemical state in all samples. The Ba peaks can be decomposed into two components at binding energies of 778.619–778.866 eV and 780.1–780.3 eV. The

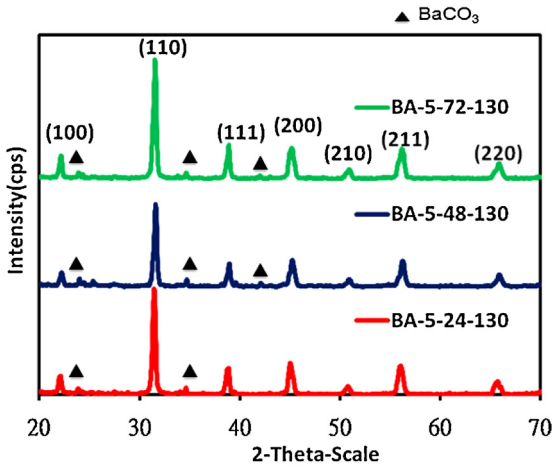

Fig. 1. XRD patterns of $BaTiO_3$ prepared using hydrothermal treatment of NaOH: (a) at 130 °C with various synthesis durations, 24 h, 48 h, 72 h ([NaOH] = 5 M) and (b) at various synthesis temperatures, 100 °C, 130 °C, 150 °C, 180 °C ([NaOH] = 5 M, synthesis time: 48 h).

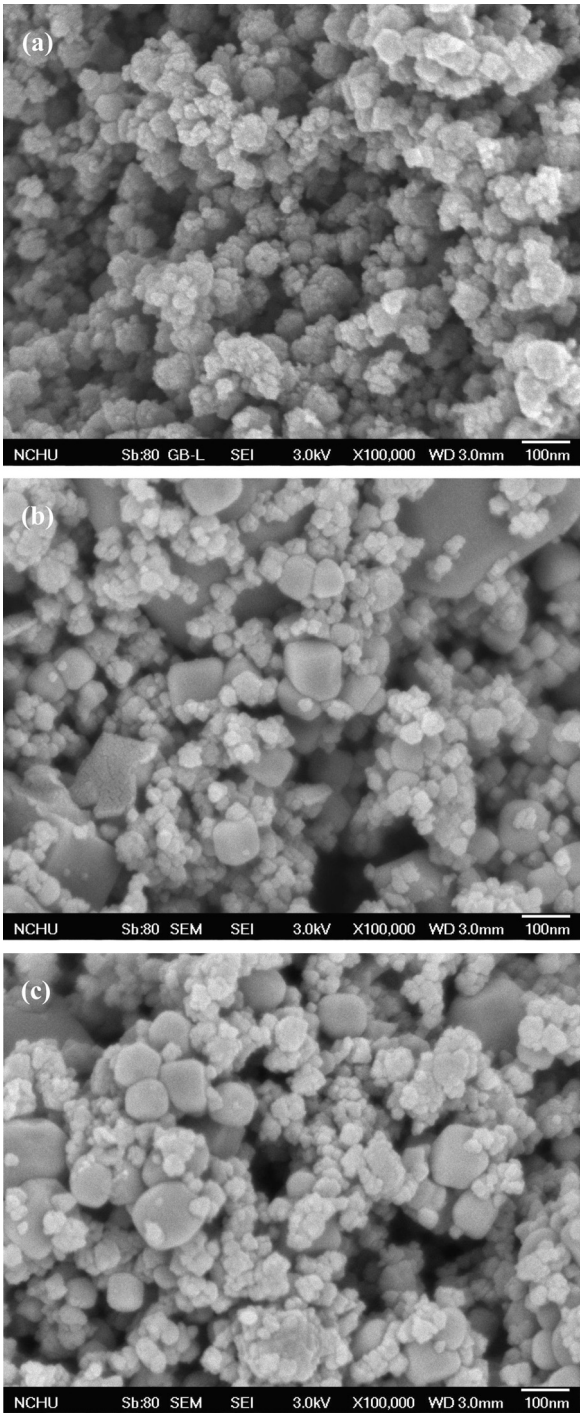

Fig. 2. FE-SEM images of $BaTiO_3$ prepared using hydrothermal treatment of NaOH at 130 °C with various synthesis durations: (a) 24 h, (b) 48 h and (c) 72 h ([NaOH] = 5 M).

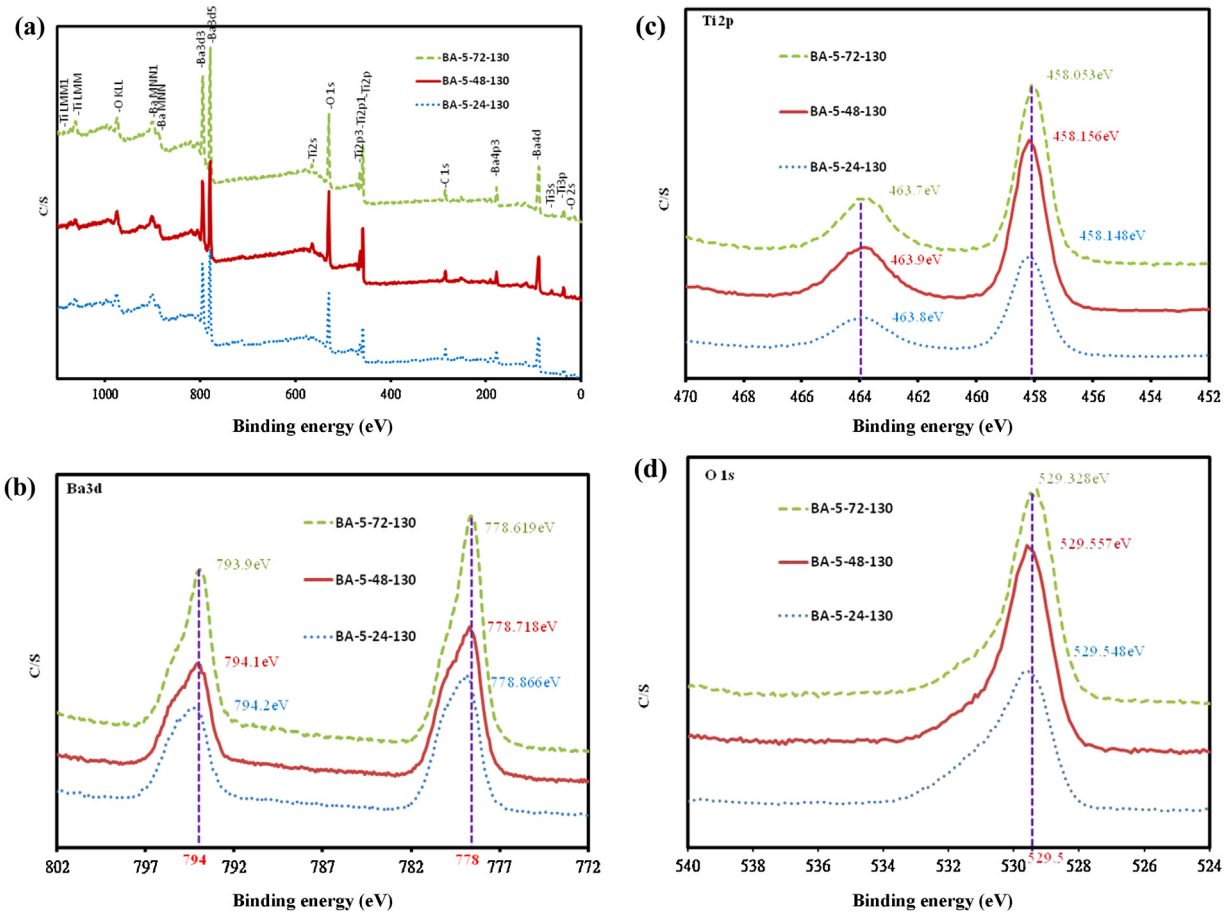

Fig. 3. High resolution XPS spectra of $BaTiO_3$ prepared using hydrothermal treatment of NaOH at 130 °C with various synthesis duration: 24 h, 48 h, 72 h ([NaOH] = 5 M). (a) Suls, (b) Ba3d, (c) Ti2p and (d) O1s.

Ba 3d state is very sensitive to all changes in structure and chemical environment, as such a transition from crystalline to amorphous phase [32] alters the number of neighboring O atoms [33] and the formation of BaO and $BaCO_3$. The first Ba 3d state component, which is the primary component of the powder XPS spectrum, can be assigned to polycrystalline $BaTiO_3$, while the presence of the second Ba 3d state component is due to a crystalline $BaCO_3$ structure.

Fig. 4 shows the FT-IR spectra produced under different synthesis durations. The characteristic absorption at 3425.0 cm^{-1} (O–H stretching modes in crystallization water) is assigned to the OH stretching vibration. The infrared spectrum of a carboxylate group, CO_3^{2-}, shows the characteristic doublet absorption due to the asymmetric and symmetric stretching vibrations at 1384.64 and 1617.98 cm^{-1} (carboxylate group stretching modes, probably $BaCO_3$), and 850 and 520 cm^{-1} (Ti–O vibrational modes) [34], respectively. A broad band corresponding to the Ti–O stretching mode for $BaTiO_3$ was also observed at approximately 590 cm^{-1} [35].

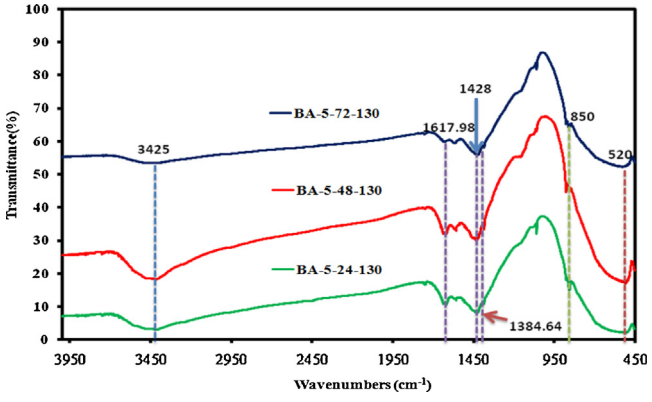

Fig. 4. FT-IR spectra of $BaTiO_3$ prepared using hydrothermal treatment of NaOH at 130 °C with various synthesis durations: 24 h, 48 h, 72 h ([NaOH] = 5 M).

As $BaTiO_3$ was a direct band gap semiconductor [36], the absorbance of the UV–vis diffuse reflectance spectrum for the nanoparticles is shown in Fig. 5. Regarding absorption threshold, we can calculate the band gap from the pattern using the equation, E_g (eV) = 1240/λ (nm). The band gap (E_g) of nano-BTO is estimated to be approximately 2.93 eV and 3.05 eV, respectively, which implies that photocatalytic properties may exist under UV-light irradiation. The band gap value reported for particles ranging from 3.1 eV to 3.2 eV [37] depends on powder and processing details.

It is known that the size of nanoparticles has a significant influence on the photocatalytic properties, due to variations in surface area, the number of active sites, *etc.* [38]. Smaller nanoparticles result in a larger surface area (more active sites) and enhance the photocatalytic activity. Moreover, the band gap energy is also correlated to photocatalytic activity [39]. A lower band gap has a positive effect on photocatalytic activity because less source energy is required to arouse a photocatalytic reaction. This means that less energy is required to activate the nanoparticles to generate excited electron/hole pairs, thereby inducing photocatalytic reactions. In addition, the specific surface area and pore volume of samples did not undergo significant changes and remained in the range of 17.88–20.85 m^2/g and 5.146–6.054 × 10^3 cm^3/g for all samples (Table 2). This suggests that

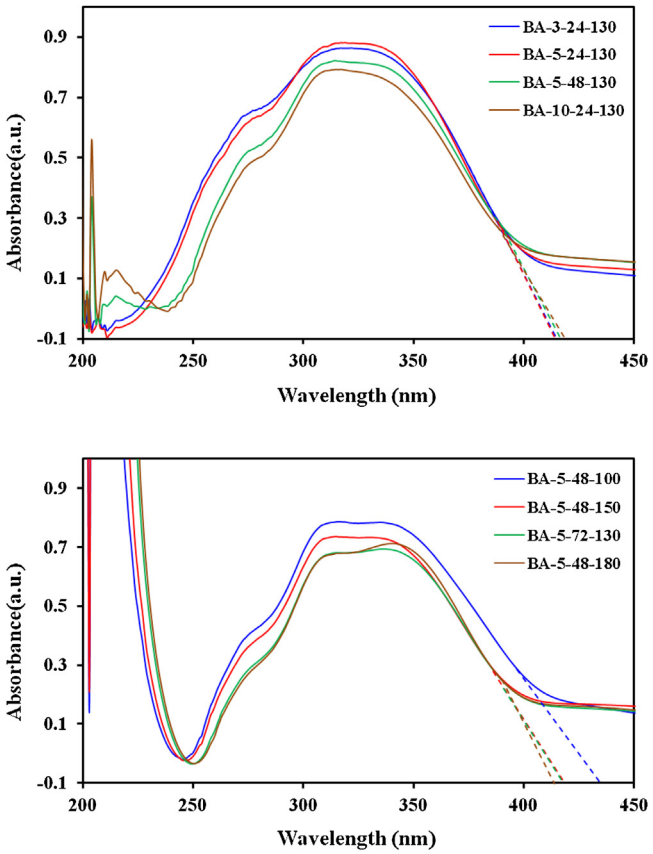

Fig. 5. UV–vis diffuse reflectance spectra of $BaTiO_3$ prepared using hydrothermal treatment with various concentrations of NaOH, synthesis duration, and temperature.

the higher photocatalytic activity of BA-5-48-130 (over that of BA-5-72-130 and BA-5-24-130) could be attributed to a lower band gap, which would lead to the generation of more excited electron–hole pairs, enhancing photocatalytic activity. Among the other $BaTiO_3$, BA-5-48-130 has the lowest band gap and the smallest particle size (larger surface area), and therefore provides the highest photocatalytic efficiency.

Fig. 6 shows the photocatalytic activity of the nanoparticles. The efficiency of photocatalytic degradation of CV is 99% for nano-BTO within the first 48 h. The adsorption reaction resulted in a decrease in CV concentration of approximately ~48% after 48 h, while in the photocatalytic reaction, the CV was completely decomposed after 48 h. In the following experiment, we selected $BaTiO_3$ synthesized over a period of 48 h as the optimal photocatalyst.

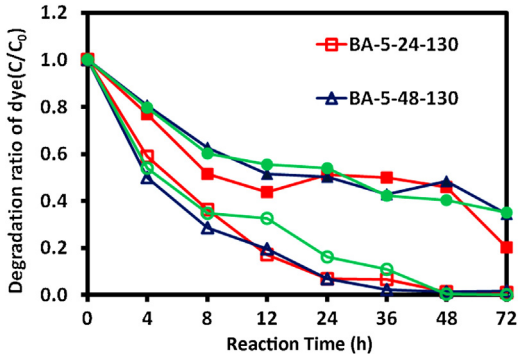

Fig. 6. Influence of UV light irradiation on the CV photodegradation rate with $BaTiO_3$ prepared using hydrothermal treatment with various synthesis durations ([catalyst] = 0.5 g/L, [CV] = 10 mg/L).

3.3. Influence of synthesis temperature

To study the influence of synthesis temperature on the phase and particle morphology of $BaTiO_3$, it was prepared at 100, 130, 150, and 180 °C while the remaining process parameters, [NaOH] = 5 M and a synthesis duration of 48 h, were held constant. The XRD patterns of $BaTiO_3$ obtained at different hydrothermal temperatures are provided in Fig. A.4. The XRD results illustrate a well-developed cubic crystalline phase as well as an increase in the intensity of the peaks with reaction temperature. There is a possibility of a decrease in the unit-cell volume and an increase in density with an increase in the reaction temperature due to the release of lattice hydroxyls [39]. The influence of synthesis temperature is presented in Table 2. Fig. 7 depicts SEM micrographs of $BaTiO_3$ prepared at 100, 130, 150, and 180 °C for 48 h. The particles agglomerated into a cubic shape, and the cubic sizes estimated from the SEM micrographs are within 20–500 nm. An increase in synthesis temperature led to an increase in cubic size, which may explain the stronger agglomeration at higher temperature. However, for the prepared $BaTiO_3$, the particle size increased with an increase in the reaction temperature, confirming that the particle size of $BaTiO_3$ is dependent on synthesis temperature. The results of SEM investigations provide strong evidence that the oriented aggregation of small (5–10 nm) nanocrystals is the dominant growth mechanism in the formation of the observed $BaTiO_3$ particles. The particle size can be tailored in the range 20–500 nm by varying the reaction duration, temperature, and concentration. The above results show that the aggregation process can be controlled by changing the temperature and concentration of the suspension as well as by adding NaOH, to obtain $BaTiO_3$ particles with a controlled size and shape.

Fig. 8 shows the photocatalytic activity of the nanoparticles. The efficiency of photocatalytic degradation of CV was 99% for nano-BTO prepared at 130 °C. The adsorption reaction resulted in a decrease of approximately 44% in CV concentration after 48 h; in the photocatalytic reaction, the CV was completely decomposed after 48 h. The optimal $BaTiO_3$ photocatalyst was produced at a NaOH concentration of 5 M, synthesis time of 48 h, and synthesis temperature of 130 °C (BA-5-48-130).

3.4. Influence of quantity of catalyst

In photocatalytic processes, the quantity of photocatalyst is an important parameter capable of influencing the degradation rate of organic compounds. Catalyst optimization depends on the nature of the powders [40]. In Fig. A.5, the rate of CV photodegradation was found to be optimal when photocatalyst (BA-5-48-130) was employed at a ratio of 0.5 g/L under pH = 9 conditions.

3.5. Influence of pH

Under the conditions of pH above pHzpc (zero point charge), the surface of the negatively charged photocatalyst easily adsorbs cationic species while, under the reverse conditions, anionic species are adsorbed [40]. The adsorption of the substrate onto the $BaTiO_3$ surface directly influences the transfer of electrons between the excited dye and $BaTiO_3$, and further influences the degradation rate. The rates of CV dye photodegradation at various pH values are shown in Fig. A.6. The photodegradation rate was found to decrease and then increase with an increase in the pH value of the solution. The formation of active $^{\bullet}OH$ species is favorable under basic conditions, not only due to the improvement in the transference of holes to the adsorbed hydroxyls at high pH conditions, but also due to the electrostatic attractive effect between the negatively charged $BaTiO_3$ film and the cationic dyes in the solution. Our results indicate that the $BaTiO_3$ surface was

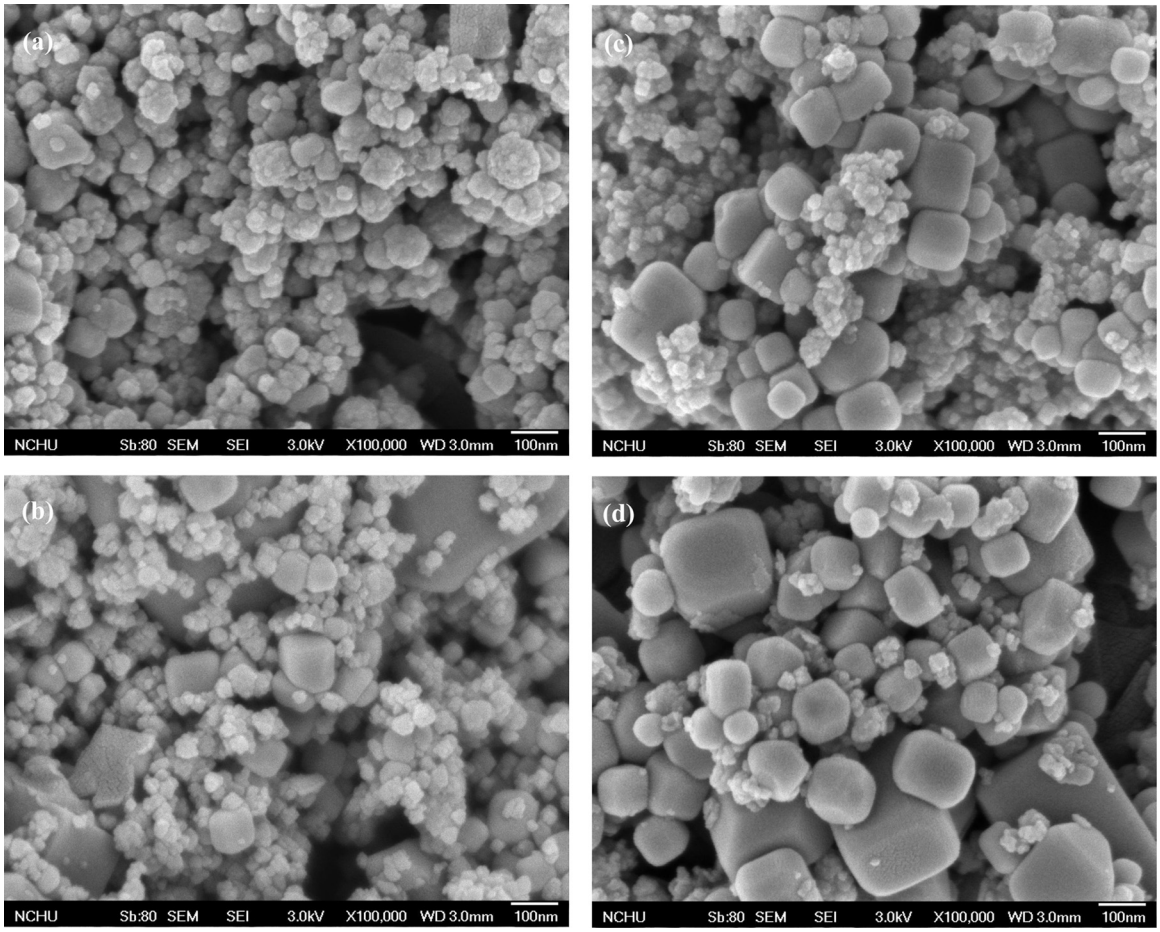

Fig. 7. FE-SEM images of $BaTiO_3$ prepared using hydrothermal treatment of NaOH at various synthesis temperatures: (a) 100 °C, (b) 130 °C, (c) 150 °C, (d) 180 °C ([NaOH] = 5 M, synthesis time: 48 h).

negatively charged, and the CV adsorbed onto the surface of the $BaTiO_3$ through the positive ammonium groups. The proposed adsorption mechanisms are in good agreement with earlier reports [41]. Although the CV dye can, to some extent, adsorb onto the surface of the $BaTiO_3$ in alkaline media, when the pH value is over 10, the dye molecule will transform into a colorless carbinol base [42]. The results related to the photodegradation rate differed from those of cationic dyes in the triphenylmethane/TiO_2 system [43].

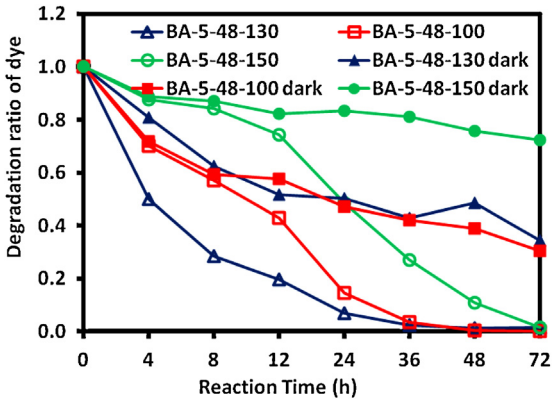

Fig. 8. Influence of UV light irradiation on CV photodegradation rate using $BaTiO_3$ prepared using hydrothermal treatment with various synthesis temperatures ([catalyst] = 0.5 g/L, [CV] = 10 mg/L).

Moreover, a higher degradation rate under acid pH is also seen for the degradation of azo dyes in TiO_2-mediated experiments due to the efficient electron-transfer process that occurs with complex surface bond formations [44]. Hydroxyl radicals can be formed by the reaction between hydroxide ions and positive holes. The positive holes are considered major oxidation species at low pH while hydroxyl radicals are the predominant species at neutral or high pH levels [45]. An additional explanation for the effect of pH is related to changes in the specification of the dye. That is, protonation or deprotonation of the dye can alter its adsorption characteristics and redox activity [46]. The adsorption resulted in decreases of 11.7%, 28.6%, and 52.1% in the CV concentration after 48 h under dark conditions. Photocatalytic efficiency was recorded under UV (365 nm) irradiation, which yielded 95.5%, 52.3%, and 98.6% for the BA-5-48-130 photocatalysts at pH = 5, 7, 9, respectively. The activity of P25 TiO_2 was more slightly than $BaTiO_3$. A coherent tendency of physical adsorption and chemical photodegradation behavior was observed in this study.

3.6. Separation and identification of intermediates

Temporal variations in the CV dye photodegradation process using UV irradiation have been characterized with HPLC-PDA-ESI–MS. The relevant changes in the chromatograms recorded at 580, 350, and 300 nm are illustrated in Fig. A.7. Following irradiation for 72 h, nineteen components were identified with retention times of less than 50 min. The CV dye and its relevant intermediates are denoted as species **A–J**, **a–f**, and **α–γ** (Table 3). Except for the initial

Table 3
Summary of the CV photocatalytic degradation intermediates identified using HPLC-PDA-ESI/MS.

HPLC peaks	De-methylation intermediates	Abbreviation	ESI/MS molecular ions (m/z)	Adsorption maximum (nm)
A	*N*, *N*, *N′*, *N′*, *N″*, *N″*-Hexamethyl-pararosaniline	CV	372.4	588.5
B	*N*, *N*-Dimethyl-*N′*, *N′*-dimethyl-*N″*-methyl-pararosaniline	DDMPR	358.4	581.2
C	*N*, *N*-Dimethyl-*N′*-methyl-*N″*-methyl-pararosaniline	DMMPR	344.4	573.9
D	*N*, *N*-Dimethyl-*N′*, *N′*-dimethyl-pararosaniline	DDPR	344.4	581.2
E	*N*-Methyl-*N′*-methyl-*N″*-methyl-pararosaniline	MMMPR	330.4	566.5
F	*N*, *N*-Dimethyl-*N′*-methyl-pararosaniline	DMPR	330.4	570.2
G	*N*-Methyl-*N′*-methyl-pararosaniline	MMPR	316.34	562.9
H	*N*, *N*-Dimethyl-pararosaniline	DPR	316.28	566.5
I	*N*-Methyl-pararosaniline	MPR	302.22	555.5
J	Pararosaniline	PR	288.39	540.9
a	4-(*N*, *N*-Dimethylamino)-4′-(*N′*, *N′*-dimethylamino)benzophenone	DDBP	269.28	377.1
b	4-(*N*, *N*-Dimethylamino)-4′-(*N′*-methylamino)benzophenone	DMBP	255.23	366.3
c	4-(*N*-Methylamino)-4′-(*N′*-methylamino)benzophenone	MMBP	241.05	362.9
d	4-(*N*, *N*-Dimethylamino)-4′-aminobenzophenone	DBP	241.27	359.9
e	4-(*N*-Methylamino)-4′-aminobenzophenone	MBP	227.37	357
f	4,4′-bis-Aminobenzophenone	BP	213.27	339
α	4-(*N*, *N*-Dimethylamino)phenol	DAP	138.23	309
β	4-(*N*-Methylamino)phenol	MAP	121.03	288.9
γ	4-Aminophenol	AP	110.97	278.2

CV dye (peak **1**), the intensities of all peaks increased at first and subsequently decreased, indicating the formation and transformation of intermediates.

The absorption spectra of each intermediate in the UV/vis spectral region are identified as peaks A–J, a–f, and α–γ in the supplementary material Fig. A.8. The most important consideration is that the hypsochromic shift of the absorption band is presumed to result from the formation of a series of *N*-de-methylated intermediates. As shown above, similar phenomena have been demonstrated using Bi_2WO_6 in the photodegradation of CV [47]. The above intermediates were identified as the same as those associated with the degradation of CV using $BaTiO_3$.

The photo-decomposed intermediates were further identified using the HPLC-ESI mass spectrometric method shown in Fig. A.9. The molecular ion peaks appeared to be in the acid form of the intermediates (supplementary material Fig. A.10). From the results of mass spectral analysis, component **A**, m/z = 372.40, was confirmed. The other components were **B**, m/z = 358.40; **C**, m/z = 344.40; **D**, m/z = 344.40; **E**, m/z = 330.40; **F**, m/z = 330.40; **G**, m/z = 316.34; **H**, m/z = 316.28; **I**, m/z = 302.22; **J**, m/z = 288.39; **a**, m/z = 269.28; **b**, m/z = 255.23; **c**, m/z = 241.05; **d**, m/z = 241.27; **e**, m/z = 227.37; **f**, m/z = 213.27; **α**, m/z = 138.23; **β**, m/z = 124.03; **γ**, m/z = 110.07. The relative distribution and time required to reach maximum concentration for the *N*-de-methylated and oxidative cleavage reaction of the conjugated chromophore structure intermediates are also illustrated. In accordance with data shown in Figs. A.8 and A.9, the successive appearance of the maximum distribution of each intermediate, such as **B–J**, **a–f**, and **α–γ**, indicates the occurrence of a stepwise process of CV *N*-de-methylation.

3.7. Proposed mechanism of CV degradation

Under UV irradiation, most of the $^{\bullet}OH$ radicals are generated directly from the reaction between the holes and surface-adsorbed H_2O or OH^-. However, the probability of the formation of $O_2^{\bullet-}$ is much lower than that of $^{\bullet}OH$ [48]. The *N*-de-methylation of the CV dyes occurs mostly by the attack of the $^{\bullet}OH$ and $O_2^{\bullet-}$ species on the *N*, *N*-dimethyl groups and the conjugated chromophore structure of the CV dye.

Conversely, especially in the $BaTiO_3$ system, the first product (**B**) of *N*-de-methylation reached maximum concentration after 4 h of irradiation (Fig. A.11, curve **B**). Further formation of intermediates, such as **C–D**, **E–F**, **G–H**, and **I–J**, reached maximum concentration after irradiation periods of 12, 12, 24, and 36–48 h, respectively (Fig. A.11, curve **C–D**, **E–F**, **G–H**, and **I–J**). In the case of the $SrTiO_3$ system, intermediates **B**, **C–D**, **E–F**, **G–H**, and **I–J**, reached maximum concentrations after irradiation for 8, 24, 24, 36, and 36 h, respectively (Fig. A.11, curve B, C–D, E–F, G–H, and I–J). The $^{\bullet}OH$ radicals attacked the mono-, di-, tri-, and tetra-methyl groups resulting in **B**, **C–D**, **E–F**, **G–H**, and **I–J** compounds, which were produced mainly during the *N*-de-methylation process. Moreover, both **a** and **α** are stepwise *N*-de-methylated, yielding compounds **f**, and **γ**. It should be emphasized that upon these mechanisms, all aforementioned processes rely on O_2 to promote the cleavage of the CV conjugated chromophore structure.

However, from the above results, the effect of different catalysts demonstrated that the formation rate of intermediates increases as the $^{\bullet}OH$ or $O_2^{\bullet-}$ concentration increases, until a critical $^{\bullet}OH$ or $O_2^{\bullet-}$ concentration is achieved. Although, photocatalytic activity strongly depends on the photocatalyst, analysis of the underlying mechanism demonstrates that a degradation pathway leads most oxidative *N*-de-alkylation processes, preceded by the formation of a nitrogen-centered radical, whereas the destruction of the dye chromophore structures is proceeded by the generation of a carbon-centered radical [47].

It is well known that the potential of multi-electron reduction of O_2 (*e.g.*, $O_2 + 2H^+ + 2e^- = H_2O_{2(aq)}$, +0.682 V; $O_2 + 4H^+ + 4e^- = 2H_2O$, +1.23 V) is more likely than for the single-electron process (*e.g.* $O_2 + e^- = O_2^{\bullet-}{}_{(aq)}$, −0.284 V; $O_2 + H^+ + e^- = HO_2^{\bullet}$, −0.046 V vs. NHE). It appears reasonable to assume that such multi-electron reduction more readily precedes on the surface of catalysts working to catalyze O_2 reduction. The high CV photodegradation activity mediated by $BaTiO_3$ is due to the promotion of the multi-electron reduction of O_2 on the catalyst rather than single-electron reduction [49].

Based on the above experimental results, the degradation pathway is tentatively proposed as depicted in Fig. 9 and Figs. A.12, and A.13. First, the cationic CV dye molecule was adsorbed on the surface of $BaTiO_3$ through charge attraction. Under UV irradiation, the conduction band electrons flow to the valence band. The hydrolysis or deprotonation reaction of CV dye yielded a nitrogen-centered radical. Once attacked by $^{\bullet}OH$ radicals, *N*-de-methylation occurred as shown in Fig. A.12. The mono-de-methylated dye, **B**, could also be adsorbed on the surface of $MTiO_3$ particles and be involved in a similar mechanistic process. However, the $^{\bullet}OH$ radicals could attack the conjugated structure, and produce a carbon-centered radical, eventually forming dye derivatives, **a** and **γ**. Moreover, the species **a** and **γ** can also be implicated in *N*-de-methylation to yield **b** and **β** (Fig. A.13), respectively. The *N*-de-methylation processes continue to form *N*-de-methylated dye, **J**, **f**

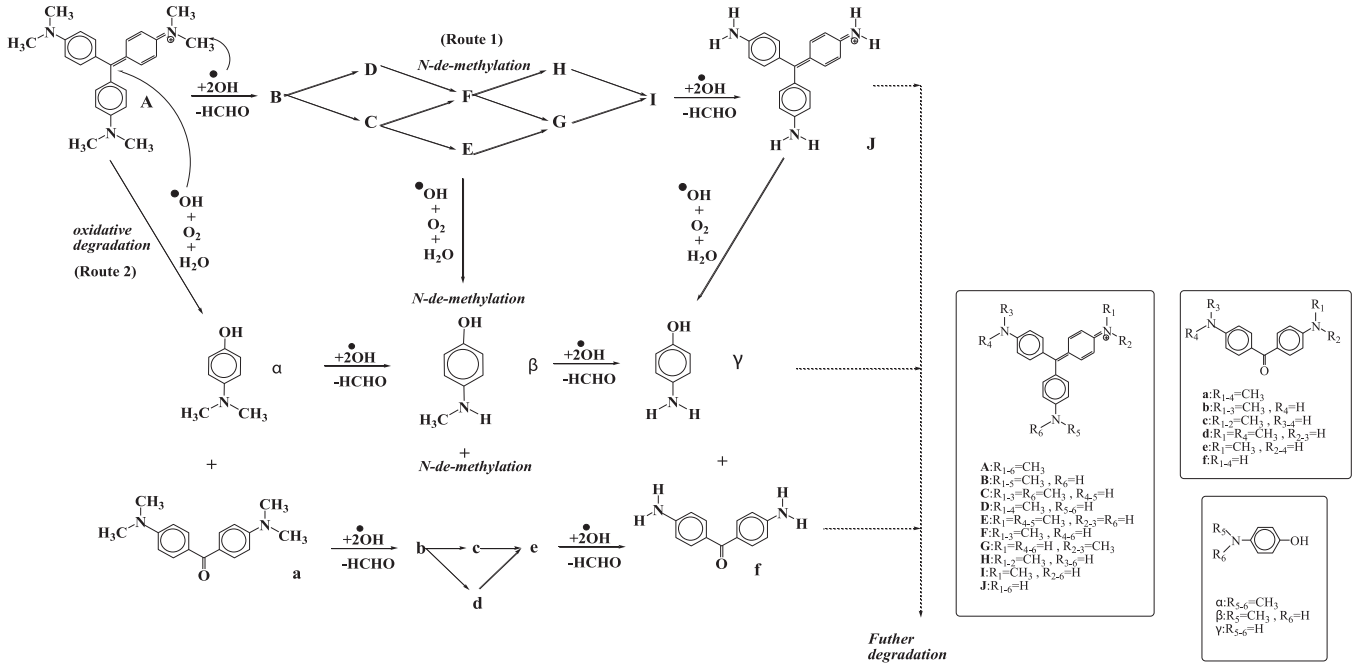

Fig. 9. Proposed mechanism involved in the photocatalytic degradation of CV using $BaTiO_3$.

and **γ**. Further oxidation can lead the ring-opening and the formation of aliphatic oxidation products [50].

4. Conclusion

Nano-cubic $BaTiO_3$ particles were obtained by hydrothermal methods using an aqueous gel suspension using P25-TiO_2, $Ba(OH)_2$, and NaOH. The results of SEM show that the aggregation process can be controlled by changing the temperature and concentration of the suspension as well as by adding NaOH, to obtain $BaTiO_3$ particles with a controlled size and shape. These results indicate that BA-5-48-130 has the highest photocatalytic activity. Most of the intermediates and final products were identified by HPLC-ESI–MS and UV–vis spectra. Both *N*-demethylation and the destruction of the conjugated structure of the CV dye took place on the $BaTiO_3$. This is the first report demonstrating the pathways of photocatalytic degradation of $BaTiO_3$ involved in the photodegradation of CV dye.

Acknowledgment

This research was supported by the National Science Council of China (NSC 99-2113-M-142-002-MY2).

Appendix A. Supplementary data

Supplementary data associated with this article can be found, in the online version, at http://dx.doi.org/10.1016/j.jtice.2013.01.005.

References

[1] Chan SHS, Wu TY, Juan JC, Teh CY. Recent developments of metal oxide semiconductors as photocatalysts in advanced oxidation processes (AOPs) for treatment of dye waste-water. J Chem Technol Biotechnol 2011;86:1130–58.
[2] Chern JM. Decolorization technologies for textile effluent treatment. J Taiwan Inst Chem Eng 2012;43:329–30.
[3] Ullmann's encyclopedia of industrial chemistry. Part A27. Triarylmethane and diarylmethane dyes, 6th ed., New York: Wiley-VCH; 2001.
[4] Lewis LM, Indig GL. Effect of dye aggregation on triarylmethane-mediated photoinduced damage of hexokinase and DNA. J Photochem Photobiol B Biol 2002;67:139–48.
[5] Cho BP, Yang T, Blankenship LR, Moody JD, Churchwell M, Bebland FA, et al. Synthesis and characterization of *N*-demethylated metabolites of Malachite Green and Leucomalachite Green. Chem Res Toxicol 2003;16:285–94.
[6] Tong H, Ouyang S, Bi Y, Umezawa N, Oshikiri M, Ye J. Nano-photocatalytic materials: possibilities and challenges. Adv Mater 2011;23:1–23.
[7] Thompson TL, Yates JT. Surface science studies of the photoactivation of TiO_2-new photochemical processes. Chem Rev 2006;106:4428–53.
[8] Tang J, Durrant JR, Klug DR. Mechanism of photocatalytic water splitting in TiO_2. Reaction of water with photoholes, importance of charge carrier dynamics, and evidence for four-hole chemistry. J Am Chem Soc 2008;130:13885–91.
[9] Lin WC, Yang WD, Jheng SY. Photocatalytic degradation of dyes in water using porous nanocrystalline titanium dioxide. J Taiwan Inst Chem Eng 2012;43:269–74.
[10] Demirörs AF, Imhof A. $BaTiO_3$, $SrTiO_3$, $CaTiO_3$, and $Ba_xSr_{1-x}TiO_3$ particles: a general approach for monodisperse colloidal perovskites. Chem Mater 2009;21:3002–7.
[11] Modeshia DR, Walton RI. Solvothermal synthesis of perovskites and pyrochlores: crystallisation of functional oxides under mild conditions. Chem Soc Rev 2010;39:4303–25.
[12] Nyutu EK, Chen CH, Dutta PK, Suib SL. Effect of microwave frequency on hydrothermal synthesis of nanocrystalline tetragonal barium titanate. J Phys Chem C 2008;112:9659–67.
[13] Liu Y, Chen G, Zhou C, Hu Y, Fu D, Liu J, et al. Higher visible photocatalytic activities of nitrogen doped In_2TiO_5 sensitized by carbon nitride. J Hazard Mater 2011;190:75–80.
[14] Song ZQ, Wang SB, Yang W, Li WM, Wang H, Hui Y. Synthesis of manganese titanate $MnTiO_3$ powders by a sol–gel–hydrothermal method. Mater Sci Eng B 2004;113:121–4.
[15] Wang H, Zhang XX, Huang AP, Xua HY, Zhu MK, Wang B, et al. A new phase of cadmium titanate by hydrothermal method. J Cryst Growth 2002;246:150–4.
[16] Chen YH, Chen YD. Kinetic study of Cu(II) adsorption on nanosized $BaTiO_3$ and $SrTiO_3$ photocatalysts. J Hazard Mater 2011;185:168–73.
[17] Pfaff GJ. Sol–gel synthesis of strontium titanate powders of various compositions. Mater Chem 1993;7:721–4.
[18] Mao YB, Banerjee S, Wong SS. Large-scale synthesis of single-crystalline perovskite nanostructures. J Am Chem Soc 2003;125:15718–19.
[19] Niederberger M, Garnweitner G, Pinna N, Antonietti M. Nonaqueous and halide-free route to crystalline $BaTiO_3$, $SrTiO_3$, and (Ba,Sr)TiO_3 nanoparticles via a mechanism involving C–C bond formation. J Am Chem Soc 2004;126:9120–6.
[20] Bansal V, Poddar P, Ahmad A, Sastry M. Room-temperature biosynthesis of ferroelectric barium titanate nanoparticles. J Am Chem Soc 2006;128:11958–63.
[21] Miyauchi M. Thin films of single-crystalline $SrTiO_3$ nanorod arrays and their surface wettability conversion. J Phys Chem C 2007;111:12440–45.
[22] Sun W, Li J. Preparation of fine tetragonal barium titanate powder by a microwave-hydrothermal process. J Am Ceram Soc 2006;89:118–23.
[23] Bao NZ, Shen LM, Srinivasan G, Yanagisawa K, Gupta A. Shape-controlled monocrystalline ferroelectric barium titanate nanostructures: from nanotubes and nanowires to ordered nanostructures. J Phys Chem C 2008;112:8634–42.
[24] Fan HJ, Huang ST, Chung WH, Jan JL, Lin WY, Chen CC. Degradation pathways of crystal violet by Fenton and Fenton-like systems: condition optimization and

intermediate separation and identification. J Hazard Mater 2009;171: 1032–44.
[25] Sun W. Particle coarsening. I. Kinetics for reversible dissolution/deposition controlled process. Acta Mater 2005;53:3329–34.
[26] Lencka MM, Riman RF. Thermodynamic modeling of hydrothermal synthesis of ceramic powders. Chem Mater 1993;5:61–70.
[27] Sun W, Pang Y, Li J, Ao W. Particle coarsening. II. Growth kinetics of hydrothermal $BaTiO_3$. Chem Mater 2007;19:1772–9.
[28] Atkins PW. Physical Chemistry, 5th ed., New York: W. H. Freeman, Company; 1994.
[29] Hsiang HI, Chang YL, Fang JS, Yen FS. Polyethyleneimine surfactant effect on the formation of nano-sized $BaTiO_3$ powder via a solid state reaction. J Alloys Compd 2011;509:7632–8.
[30] Guo L, Luo H, Gao J, Guo L, Yang J. Microwave hydrothermal synthesis of barium titanate powders. Mater Lett 2006;60:3011–4.
[31] Adireddy S, Lin C, Cao B, Zhou W, Caruntu G. Solution-based growth of monodisperse cube-like $BaTiO_3$ colloidal nanocrystals. Chem Mater 2010;22:1946–8.
[32] Ehre D, Cohen H, Lyahovitskaya V, Lubomirsky I. X-ray photoelectron spectroscopy of amorphous and quasiamorphous phases of $BaTiO_3$ and $SrTiO_3$. Phys Rev B 2008;77:184106–111.
[33] Van der Heide PAW. Surface core level shifts in photo-electron spectra from the Ca, Sr and Ba titanates. Surf Sci 2001;490:619–26.
[34] Tsay J, Fang T. Effects of the molar ratio of citric acid to cations and the pH value on the formation of the barium titanate citrate and its thermal decomposition behavior. J Am Ceram Soc 1999;82:1409–15.
[35] Yu P, Cui B, Shi Q. Preparation and characterization of $BaTiO_3$ powders and ceramics by sol–gel process using oleic acid as surfactant. Mater Sci Eng A 2008;473:34–41.
[36] Ashiri R, Nemati A, Ghamsari MS, Aadelkhani H. Characterization of optical properties of amorphous $BaTiO_3$ nanothin films. J Non-Cryst Solids 2009;355:2480–4.
[37] Colmenares JC, Aramendia MA, Marinas A, Marinas JM, Urbano FJ. Synthesis, characterization and photocatalytic activity of different metal-doped titania systems. Appl Catal A 2006;306:120–7.
[38] Diebold U. The surface science of titanium dioxide. Surf Sci Rep 2003;48:53–229.
[39] Qi L, Lee BI, Badheka P, Wang LQ, Gilmour P, Samuels WD, et al. Low-temperature paraelectric-ferroelectric phase transformation in hydrothermal $BaTiO_3$ particles. Mater Lett 2005;59:2794–8.
[40] Parra S, Stanca SE, Guasaquillo I, Thampi KR. Photocatalytic degradation of atrazine using suspended and supported TiO_2. Appl Catal B Environ 2004;51:107–16.
[41] Li X, Liu G, Zhao J. Two competitive primary processes in the photodegradation of cationic triarylmethane dyes under visible irradiation in TiO_2 dispersions. New J Chem 1999;23:1193–6.
[42] Chen CC, Lu CS. Mechanistic studies of the photocatalytic degradation of methyl green: an investigation of products of the decomposition processes. Environ Sci Technol 2007;41:4389–96.
[43] Konstantinou IK, Albanis TA. TiO_2-assisted photocatalytic degradation of azo dyes in aqueous solution: kinetic and mechanistic investigations: a review. Appl Catal B Environ 2004;49:1–14.
[44] Bandara J, Mielczarski JA, Kiwi J. 2. Photosensitized degradation of azo dyes on Fe, Ti, and Al oxides. Mechanism of charge transfer during the degradation. Langmuir 1999;15:7680–7.
[45] Lucarelli L, Nadtochenko V, Kiwi J. Environmental photochemistry: quantitative adsorption and FTIR studies during the TiO_2-photocatalyzed degradation of orange II. Langmuir 2000;16:1102–8.
[46] Neppolian B, Choi HC, Sakthivel S, Arabindoo B, Murugesan V. Solar light induced and TiO_2 assisted degradation of textile dye reactive blue 4. Chemosphere 2002;46:1173–81.
[47] Liao YH, Wang JX, Lin JS, Chung WH, Lin WY, Chen CC. Synthesis photocatalytic activities and degradation mechanism of Bi_2WO_6 toward crystal violet dye. Catal Today 2011;174:148–59.
[48] Chen CC, Lu CS. Photocatalytic degradation of Basic Violet 4: degradation efficiency, product distribution, and mechanisms. J Phys Chem C 2007;111:13922–32.
[49] Hirakawa T, Nosaka Y. Properties of $O_2^{\bullet-}$ and $OH^{\bullet}$ formed in TiO_2 aqueous suspensions by photocatalytic reaction and the influence of H_2O_2 and some ions. Langmuir 2002;18:3247–54.
[50] Fan H, Lu C, Jan J, Chiou M, Chen CC. Mechanistic pathways differences between P25-TiO_2 and Pt-TiO_2 mediated CV photodegradation. J Hazard Mater 2011;185:227–35.